

Model of self-generated magnetic field generation from relativistic laser interaction with solid targets

Rui Yan(严睿), De-Bin Zou(邹德滨), Na Zhao(赵娜), Xiao-Hu Yang(杨晓虎), Xiang-Rui Jiang(蒋祥瑞), Li-Xiang Hu(胡理想), Xin-Rong Xu(徐新荣), Hong-Yu Zhou(周泓宇), Tong-Pu Yu(余同普), Hong-Bin Zhuo(卓红斌), Fu-Qiu Shao(邵福球), and Yan Yin(银燕)

Citation: Chin. Phys. B, 2024, 33 (**5**): 055203. DOI: 10.1088/1674-1056/ad333f
Journal homepage: http://cpb.iphy.ac.cn; http://iopscience.iop.org/cpb

What follows is a list of articles you may be interested in

Characteristics of the electromagnetic wavepropagation inmagnetized plasma sheath and practical methodfor blackout mitigation

Xiang Wu(吴翔), Jiahui Zhang(张珈珲), Guoxiang Dong(董果香), and Lei Shi(石磊)
Chin. Phys. B, 2024, 33 (**5**): 055201. DOI: 10.1088/1674-1056/ad24d4

Probing the peripheral self-generated magnetic field distribution in laser-plasma magnetic reconnection with Martin—Puplett interferometer polarimeter

Ya-Peng Zhang(张雅芃), Jia-Wen Yao(姚嘉文), Zheng-Dong Liu(刘正东), Zuo-Lin Ma(马作霖), and Jia-Yong Zhong(仲佳勇)
Chin. Phys. B, 2024, 33 (**4**): 045206. DOI: 10.1088/1674-1056/ad24db

Wave field structure and power coupling features of blue-core helicon plasma driven by various antenna geometries and frequencies

Chao Wang(王超), Jia Liu(刘佳), Lei Chang(苌磊), Ling-Feng Lu(卢凌峰), Shi-Jie Zhang(张世杰), and Fan-Tao Zhou(周帆涛)
Chin. Phys. B, 2024, 33 (**3**): 035201. DOI: 10.1088/1674-1056/ad1486

Effects of plasma radiation on the nonlinear evolution of neo-classical tearing modes in tokamak plasmas with reversed magnetic shear

Shuai Jiang(姜帅), Zheng-Xiong Wang(王正汹), Lai Wei(魏来), and Tong Liu(刘桐)
Chin. Phys. B, 2023, 32 (**10**): 105203. DOI: 10.1088/1674-1056/acedf7

Parametric decay instabilities of lower hybrid waves on CFETR

Taotao Zhou(周涛涛), Nong Xiang(项农), Chunyun Gan(甘春芸), Guozhang Jia(贾国章), and Jiale Chen(陈佳乐)
Chin. Phys. B, 2022, 31 (**9**): 095201. DOI: 10.1088/1674-1056/ac67c2

Model of self-generated magnetic field generation from relativistic laser interaction with solid targets

Rui Yan(严睿)[1], De-Bin Zou(邹德滨)[2,†], Na Zhao(赵娜)[3], Xiao-Hu Yang(杨晓虎)[4], Xiang-Rui Jiang(蒋祥瑞)[2], Li-Xiang Hu(胡理想)[2], Xin-Rong Xu(徐新荣)[2], Hong-Yu Zhou(周泓宇)[2], Tong-Pu Yu(余同普)[2], Hong-Bin Zhuo(卓红斌)[5], Fu-Qiu Shao(邵福球)[2], and Yan Yin(银燕)[2,‡]

[1] *Northwest Institute of Nuclear Technology, Xi'an* 710024, *China*
[2] *Department of Physics, National University of Defense Technology, Changsha* 410073, *China*
[3] *School of Microelectronics and Physics, Hunan University of Technology and Business, Changsha* 410205, *China*
[4] *Department of Nuclear Science and Technology, National University of Defense Technology, Changsha* 410073, *China*
[5] *College of Engineering Physics, Shenzhen Technology University, Shenzhen* 518118, *China*

(Received 14 December 2023; revised manuscript received 23 February 2024; accepted manuscript online 13 March 2024)

Generation of self-generated annular magnetic fields at the rear side of a solid target driven by relativistic laser pulse is investigated by using theoretical analysis and particle-in-cell simulations. The spatial strength distribution of magnetic fields can be accurately predicted by calculating the net flow caused by the superposition of source flow and return flow of hot electrons. The theoretical model established shows good agreement with the simulation results, indicating that the magnetic-field strength scales positively to the temperature of hot electrons. This provides us a way to improve the magnetic-field generation by using a micro-structured plasma grating in front of the solid target. Compared with that for a common flat target, hot electrons can be effectively heated with the well-designed grating size, leading to a stronger magnetic field. The spatial distribution of magnetic fields can be modulated by optimizing the grating period and height as well as the incident angle of the laser pulse.

Keywords: self-generated magnetic field, laser solid-target interaction, micro-structured plasma grating

PACS: 52.38.Fz, 52.38.–r, 42.79.Dj **DOI:** 10.1088/1674-1056/ad333f

1. Introduction

Development of laser technologies has paved the way for generation of extremely strong magnetic fields in laboratory. Magnetic field as high as $\sim$100 MG can be obtained by laser interaction with matter.[1–7] Such a strong magnetic field environment is of great significance for investigating fundamental physics of magnetized plasmas, laboratory astrophysics, inertial confinement fusion, and production of high quality charged particles.[8–13] Relativistic laser pulse interacting with a solid target is a promising approach to excite intense magnetic fields. Interaction dynamics and generation mechanism of magnetic fields involved have attracted extensive attention due to tight correlation with collimating charged particle beams[14–16] and simulating magnetic reconnection process.[17,18] For typical ultraintense ($> 10^{18}$ W/cm^2) short ($<$ ps) laser pulse, annular self-generated magnetic fields in opposite directions can be induced on the front and rear surfaces of solid target.[3] The magnetic field on the front surface results from the hydrodynamic force, which originates from fast electrons before the target escaping into the vacuum.[19] In contrast, it has been demonstrated theoretically and in experiments that the excitation of annular magnetic fields on the back of the target can be attributed to the electron recycling at the plasma boundary.[20] This field is intense enough to cause the electrons to become strongly magnetized.[3] The lines of magnetic force are frozen in the electron fluid and tend to confine the plasma, which may reduce the divergence angle of the emitted proton or positron beams.[3]

Up to date, several theoretical models have been built to recognize the underlying physical nature of magnetic field generation in the laser target interaction.[19,21–25] For instance, Sudan found by an analytical modeling that very high dc magnetic fields on the front surface are intrinsically from spatial gradients and non-stationary character of the ponderomotive force.[19] Macchi established a model of the 'fountain' effect to interpret $\sim$100 MG magnetic field generation behind a solid target measured in the experiments at laser intensities ($> 10^{19}$ W/cm^2).[24] Nakatsutsumi thought the inductive generation of the strong B-field [$\sim$1000 MG at laser intensities ($> 10^{21}$ W/cm^2)] is mainly determined by the spatio-temporal variations of the longitudinal sheath field.[26] In fact, since this extremely high dc magnetic field is generated by the motion of hot electrons, the density and energy of the electrons determine the upper limit of the magnetic field strength, so the detailed dynamic analysis of the electrons behind the target is valuable. Although Macchi's model is simple, it captures the essential factor of current-generated magnetic field and is suitable for studying the interaction of laser with targets on the

†Corresponding author. E-mail: debinzou@nudt.edu.cn
‡Corresponding author. E-mail: yyin@nudt.edu.cn

© 2024 Chinese Physical Society and IOP Publishing Ltd

order of several micrometers. However, the contribution of radial surface return current on the rear surface is not included in these models. A satisfactory physical understanding for generation of magnetic fields at the rear side of a solid target is thus still lacking.

In this study, we develop a model capable to calculate the generation of magnetic fields behind the target by simultaneously considering the comprehensive effect of the axial net flow and radial surface return one. The spatial strength distribution of magnetic fields can be quantitatively evaluated for different laser intensities, which shows good agreement with that from the two-dimensional (2D) particle-in-cell (PIC) simulations. Our analytical scaling law indicates that the maximum strength of self-generated annular magnetic fields at the side of the solid target grows exponentially with increasing hot-electron temperature. This provides us a way to enhance the magnetic field strength. With a well-designed grating target, the hot-electron temperature is significantly improved due to efficient energy coupling from laser to target. As a result, the strength of magnetic fields can be several times enhanced compared to that of the polished target. This method is robust for different laser plasma parameters. It is found that the optimal period of the grating is close to a laser wavelength and the magnetic field strength becomes larger with increasing grating height. Moreover, the magnetic-field shows a typical radial asymmetrical spatial distribution when the laser pulse is obliquely incident on the grating target and most suitable incident angle is about 45°.

2. Results

2.1. Model of laser-induced self-generated annular magnetic field generation

Figure 1(a) shows the sketch of laser-driven self-generated magnetic field generation. When a relativistic linearly polarized laser pulse interacts with a solid target, a large number of hot electrons with an intrinsic divergence angle θ_d are produced on the front surface.[27] These electrons, acting like a fountain,[15,28] travel backwards through the rear surface of the target with its maximal beam radius r_0. Then they try to escape into the vacuum behind and form a diverging hot-electron current $\boldsymbol{J}_d$. It should be noted that $\boldsymbol{J}_d$ is actually partially compensated since the sheath electric field $\boldsymbol{E}_s$ established by these electrons tend to drag them back.[29] On this basis, Macchi proposed a fountain model to analyze the current $\boldsymbol{J}_d$.[24] However,the landing points on the rear surface of the target may deviate from the axial direction since they have radial velocity component. This results in the presence of the radial surface current components $\boldsymbol{J}_r$ when they converge toward the center. $\boldsymbol{J}_r$ will form a closed current loop with $\boldsymbol{J}_d$ along with the cold electron return one. As a result, strong annular magnetic fields around the direction of the laser propagation behind the target $\boldsymbol{B}$ will be excited by $\boldsymbol{J}_d$ and $\boldsymbol{J}_r$.

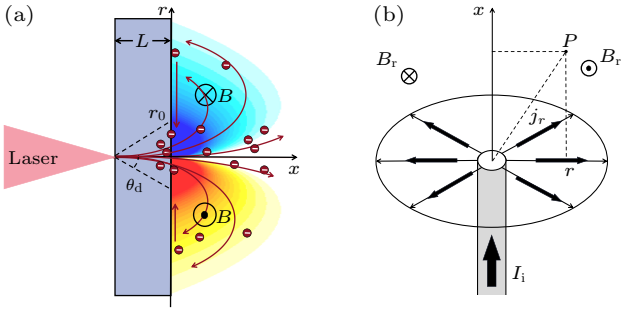


Fig. 1. (a) Schematic of the annular self-generated magnetic field generation induced by relativistic linearly polarized laser pulse. The red lines represent the trajectories of some hot electrons. Energetic hot electrons may eventually detach the targets, while some low energy electrons will be reflected back to the target by the sheath electric field. The driving current and surface net return currents will be induced in the opposite direction of the electron motion since the electrons are negatively charged. The annular self-generated magnetic fields behind the target are thus excited by the total net currents. (b) Schematic diagram for calculating the magnetic field formed by radial currents in space.

We now establish a theoretical model about $\boldsymbol{J}_d$ and $\boldsymbol{J}_r$ to calculate the spatial distribution of the strength of self-generated magnetic fields behind the target. Assume that the axis of the current is in the $\boldsymbol{x}$ direction and the thickness of the solid target is L. The rear surface of the target is located at the plane of $x = 0$ and thus the vacuum space behind the target corresponds to the spatial region of $x > 0$, which is denoted as x^+ in the following. Considering that the current is symmetric with respect to the x axis, the cylindrical coordinates (x, r, φ) are more convenient. Thus, r can represent the specific position at the plane of $x = 0$. At any point on the surface $x = 0$, the total longitudinal net flow $J_d(r)$ is the difference between the outgoing source flow $J_\uparrow(r)$ and the downward flow $J_\downarrow(r)$. Macchi analyzed a "geometrical" model of a fountain to evaluate the net flow $J_d(r)$ on the ground resulting from the superposition of the source and the falling streams,[24] $J_d(r)$ can be expressed as[24]

$$J_d(r) = J_\uparrow(r) - J_\downarrow(r) = \begin{cases} J_0\left(1-\frac{1}{C_0^2}\right)\left(1-\frac{r^2}{r_0^2}\cdot\frac{1+C_0^2}{C_0^2}\right), & 0 \le r \le r_0, \\ -J_0\frac{1}{C_0^2}\left(1-\frac{r^2}{C_0^2 r_0^2}\right), & r_0 \le r \le C_0 r_0. \end{cases} \quad (1)$$

Our work is to calculate the theoretical value of the parameter. For simplicity, the outgoing source current at point r on the plane $x = 0$ can be expressed as $J_\uparrow(r) = J_0(1 - r^2/r_0^2)$, where $J_0 = en_h v_h$ is the maximum current along the $\boldsymbol{x}$ direction, n_h and v_h are the number density and averaged velocity of hot electrons. In the electrostatic plasma expansion model,[30,31] $n_h = n_e \exp[-(x/c_s t + 1)]$, where n_e is the electron density of target, k is the Boltzmann constant, T_h is the temperature of hot electrons, $c_s = \sqrt{Z_i k T_h / m_i}$ is the ion sound speed, m_i and Z_i are the rest mass and charge of ions, respectively. Using $kT_h = (\gamma - 1)\cdot m_e c^2$ and $\gamma = 1/\sqrt{1 - v_h^2/c^2}$, we can obtain

$v_h = \sqrt{(\gamma+1)kT_h/\gamma^2 m_e}$, where γ is the relativistic factor. Taking $x = v_h t$, $n_h = n_e \exp[-(v_h/c_s+1)]$ and J_0 can thus be given by

$$J_0 = en_e \exp\left[-\left(\sqrt{\frac{(\gamma+1)m_i}{\gamma^2 Z_i m_e}}+1\right)\right]\sqrt{\frac{(\gamma+1)kT_h}{\gamma^2 m_e}}. \quad (2)$$

In the following, we use Eqs. (1) and (2) to calculate the theoretical value of the current. For the thrown electrons with averaged velocity v_h, the distance between the landing point and the center on the plane of $x = 0$ can be written as $r' = r + (2\gamma m_e v_h^2/eE_S)rL/(r^2+L^2)$. Since $r^2 \ll r_0^2 \ll L^2$ (*i.e.*, $\theta_d = 1$), r' can be approximated to $r' \approx C_0 r$, where $C_0 = 1+2\gamma m_e v_h^2/eE_S L \approx 1+2\gamma m_e v_h^2\theta_d/eE_S r_0$ is the constant. It is found that $J_d(r) > 0$ for $0 \le r < r_a = \sqrt{r_0^2 C_0^2/(1+C_0^2)}$ and $J_d(r) \le 0$ in the range of $r_a \le r < C_0 r_0$. The magnetic field B_d from $J_d(r)$ is thus strongest at $r = r_a$ since an inverse magnetic field will be excited by the negative current of $J_d(r) < 0$ for larger r. From the Biot–Savart law, we have

$$B_d(r,\varphi) = \frac{\mu_0}{2\pi r}\int_0^{2\pi} d\varphi \int_0^r J_d(r) r\, dr. \quad (3)$$

Similarly, by choosing the different landing planes in the space of $x > 0$, we can obtain the general formation

$$B_d(x,r,\varphi) = \frac{\mu_0}{2\pi r}\int_0^{2\pi} d\varphi \int_0^r J_d(r,x) r\, dr. \quad (4)$$

We next consider the contribution of J_r to the magnetic field generation. J_r is in an axisymmetric radial circular distribution with its inner and outer radii $r = r_a$ and $C_0 r_0$ on the plane of $x = 0$, as shown in Fig. 1(b). The total radial return current can be obtained by integrating

$$I_r = \int_0^{2\pi} d\varphi \int_{r_a}^{C_0 r_0} J_r(r) r\, dr. \quad (5)$$

Obviously, $\boldsymbol{J}_r$ will form a radial magnetic field B_r with the same spatial distribution as B_d. To conveniently calculate B_r by generated by $\boldsymbol{J}_r$, we assume that $\boldsymbol{J}_r$ is sprayed out from a semi-infinite $(-\infty, 0)$ linear current I_i equal to I_r, and I_i does not affect the distribution of $\boldsymbol{J}_r$. The magnetic field B_i generated by I_i can be given by $B_i = -(\mu_0 I_i/4\pi r)(1 - x/\sqrt{r^2+x^2})$.[32] For any point $P(x,r)$ in the x^+ space, $\oint_L B_0\, dl = B_0 \cdot 2\pi r = 0$ from Ampere loop theorem and thus $B_0 = 0$, where B_0 is the total magnetic field of I_r and I_i. According to the superposition principle of the fields $B_0 = B_i + B_r$, we have

$$B_r = \frac{\mu_0 I_r}{4\pi r}\left(1 - \frac{x}{\sqrt{r^2+x^2}}\right). \quad (6)$$

Since the magnetic fields from $J_d(r)$ and $J_r(r)$ are in the same direction, by combining Eqs. (4) and (6), the strength of total excited magnetic field B behind the target is

$$B = \frac{\mu_0}{2\pi r}\int_0^{2\pi} d\varphi \int_0^r J_d(r,x) r\, dr + \frac{\mu_0 I_r}{4\pi r}\left(1 - \frac{x}{\sqrt{r^2+x^2}}\right). \quad (7)$$

The maximum B_d and B_r on the rear surface of target (i.e., $x = 0$) is at $r = r_a$. The maximum longitudinal, radial and total magnetic fields can thus be given by

$$B_{d,max} = \mu_0 \frac{\gamma m_e v_h^2}{eE_S} J_0 \theta_d = \left(1+\frac{1}{\gamma}\right)\frac{\mu_0 J_0 kT_h \theta_d}{eE_S}, \quad (8)$$

$$B_{r,max} \approx \frac{7}{10}\left(1+\frac{1}{\gamma}\right)\frac{\mu_0 J_0 kT_h \theta_d}{eE_S}, \quad (9)$$

$$B_{max} = B_{d,max} + B_{r,max} \approx 1.7\left(1+\frac{1}{\gamma}\right)\frac{\mu_0 J_0 kT_h \theta_d}{eE_S}. \quad (10)$$

In the freely expansion plasma model, the sheath accelerating field behind the target is $E_S = kT_h/ec_s t$ for a single-species ion target.[33] In a two-species plasma target case, E_S beyond the heavy-ion front can be expressed as[34]

$$E_S' = \frac{\sqrt{2}kT_h}{e\lambda_{D,f}} e^{e\phi_0/2kT_h}\left[1 + \frac{(x-x_i)}{\sqrt{2}\lambda_{D,f}} e^{e\phi_0/2kT_h}\right]^{-1}, \quad (11)$$

where $\lambda_{D,f}$ is the hot-electron Debye length, ϕ_0 is the electric potential at the location of heavy ions, x and x_i are the positions of the light- and heavy-ion fronts, respectively. In the initial stage in which heavy ions have not responded (i.e., $x_i = 0$), E_S' reaches its maximal value when $\phi_0 = 0$, we have

$$E_S' = \frac{kT_h}{e(\lambda_D + x)} \approx \frac{kT_h}{ec_{s,l}t}, \quad (12)$$

where $c_{s,l} = \sqrt{Z_{i,l}kT_h/m_{i,l}}$ is the sound speed of light ions. E_S' is thus consistent with that in the freely expansion plasma model. Taking $\theta_d = \tan^{-1}\sqrt{2/(\gamma-1)}$[27] and $t = \tau_0$, the maximum magnetic field can be calculated by

$$B_{max} \approx \left(1+\frac{1}{\gamma}\right)\sqrt{\frac{ZkT_h}{m_i}}\tan^{-1}\sqrt{\frac{2}{(\gamma-1)}}\, 1.7\mu_0 J_0 \tau_0. \quad (13)$$

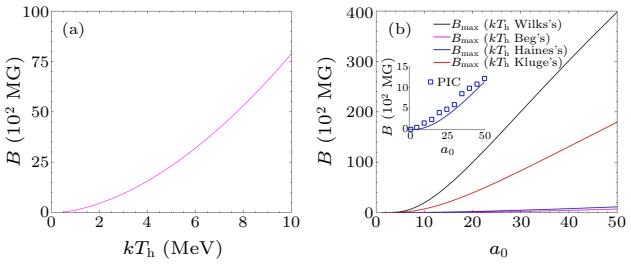


Fig. 2. Dependence of the maximum magnetic field B_{max} on (a) the temperature of hot electrons kT_h and (b) the normalized laser amplitude a_0 for several existing scalings of the hot-electron temperature. The inset in (b) shows the comparison between B_{max} from PIC simulations and that obtained by Eq. (13) based on Haines scaling.

Figure 2(a) shows the maximum magnetic field strength B_{max} versus kT_h. We can see that B_{max} rises rapidly with increasing kT_h. This provides us a way to enhance the strength of self-generated annular magnetic field behind the target, i.e., with increasing kT_h. For instance, we can increase the laser intensity to enhance the magnetic field generation since kT_h

scales as a_0^n (here $n > 0$) under different laser-target conditions, where $a_0 = eE_L/m_e\omega_L c$ is the normalized laser amplitude, e and m_e are the electron charge and mass, E_L and ω_L are the electric field and frequency of the laser, respectively.

Figure 2(b) shows the dependence of B_{max} on the laser amplitude a_0 for several existing scalings of the hot-electron temperature, including Wilks's ponderomotive force scaling[29] $kT_h = [(1 + a_0^2)^{1/2} - 1]m_e c^2$, Beg's empirical scaling[35] $kT_h = 0.47a_0^{2/3}m_e c^2$, Haines's relativistic scaling[36] $kT_h = [(1 + 2^{1/2}a_0)^{1/2} - 1]m_e c^2$, Kluge's weighted average scaling[37] $kT_h = [\pi/2K(-a_0^2) - 1]m_e c^2$, where $K(-a_0^2)$ is the complete elliptical integral of the first kind. Here, Wilks's scaling is based on the theory that the temperature of hot electrons is equal to the ponderomotive force potential of the laser.[29] Beg's scaling is from the experimental diagnostic result that the temperature of hot electrons is significantly lower than that of Wilks's scaling.[35] Haines *et al.*[36] explained why this difference occurs, which is attributed to the fact that the distance of hot electrons travelling forward in a laser cycle is greater than the skin depth of the laser, so the electrons cannot acquire the full ponderomotive potential. In addition, in order to accurately calculate the hot electron temperature, Kluge *et al.* also obtained the exact solution under both non-relativistic and relativistic conditions by means of the weight average of the kinetic energy of a large number of electrons.[37] For all the hot electron scalings, we find that B_{max} grows almost exponentially with increasing a_0. In the Wilks scaling case, B_{max} is even as high as 1×10^4 MG at $a_0 = 20$.

2.2. Simulation validation of magnetic field generation model

We perform the 2D-PIC simulations to verify the above analytical model. A p-polarized laser pulse is normally incident along the x axis ($\theta = 0$) and is focused at the front surface of the target. Its spatio-temporal profile is given by $a = a_0 \sin^2(\pi t/2\tau_0)\exp(-r^2/r_0^2)$, where $a_0 = 10$, and $\tau_0 = 10T_0$ and $r_0 = 3\lambda_0$ are the pulse duration and the focal spot radius of the laser, respectively. The target of thickness $L_0 = 3\lambda_0$ is fully ionized with the electron and ion densities of $n_e = 7n_p = 7n_{C^{6+}} = 70n_c$, which is located between $x = 10\lambda_0$ and $x = 13\lambda_0$. Here, n_e, n_p and $n_{C^{6+}}$ are the electron, proton and C^{6+}-ion densities, $n_c = m_e\omega_0{}^2/4\pi e^2$ is the critical plasma density, and ω_0 is the central frequency of laser.

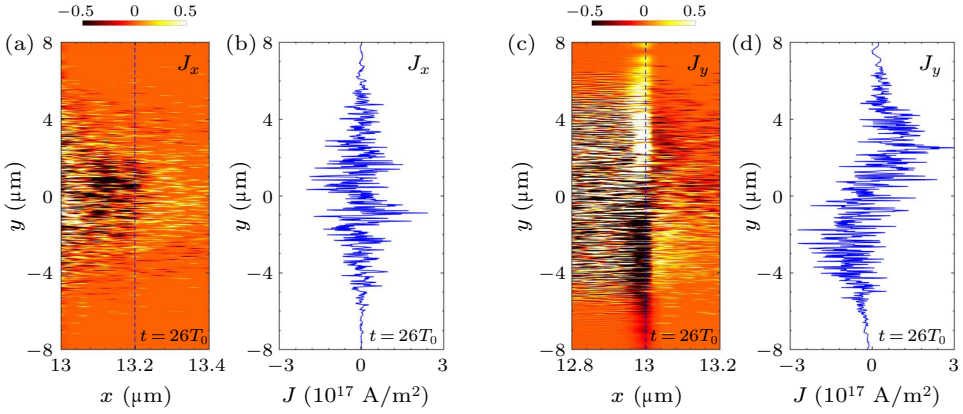


Fig. 3. Distributions of (a) longitudinal current density J_x and (c) transverse current density J_y at $t = 26T_0$ and their profiles along the $x = 13.2$ μm axis [(b) J_x; (d) J_y] from PIC simulations.

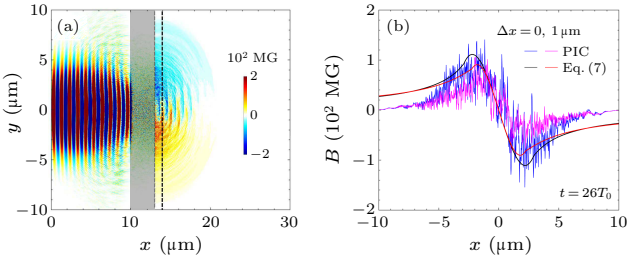


Fig. 4. (a) Distributions of self-generated magnetic field B_z at $t = 26T_0$ and (b) its transverse profiles along both axes $\Delta x = 0$ μm and 1 μm from the rear surface of the target from PIC simulation [$\Delta x = 0$ μm: blue curves; $\Delta x = 1$ μm: pink curves] and Eq. (7) [$\Delta x = 0$ μm: black curves; $\Delta x = 1$ μm: red curves].

Figure 3 shows the distributions of the longitudinal and transverse current density at $t = 26T_0$ and their profiles along the $x = 13.2$ μm axis. We can see from Figs. 3(a) and 3(b) that there are positive ($J_\uparrow$) and negative ($J_\downarrow$) current components for both J_x and J_y since the hot electrons will be transported forth and back by the sheath electric field E_S. In addition, some slightly lower-energy hot electrons will fall down to either side of the $+y$-axis due to their inherent divergence angle. With the cold electron return current in the target, this leads to the fact that J_y (or J_r in 3D geometry) is greater than 0 in the $+y$ direction and is below 0 in the $-y$ direction. As a whole, the electron current distribution described in the above theoretical model is consistent with that in PIC simulation.

Figure 4(a) shows the distribution of magnetic field strength B_z from PIC simulation. One can see that self-generated annular magnetic field is indeed produced on the back of the target. Its transverse profiles along both axes $\Delta x = 0$ μm and 1 μm from the rear surface of the target can be seen in Fig. 4(b). We find that they agree well with that

of Eq. (7) in terms of both the whole spatial distributions and their maximum values. It needs to be noted that, because J_r is assumed to be distributed on the whole plane $x = 0$ when we calculate it, there exists an overestimation of the magnitude of the magnetic field in regions where $\Delta y < -5$ μm and $\Delta y > 5$ μm, and this result does not affect the estimation of other regions. The simulations with different laser amplitude a_0 are performed. As shown in the inset of Fig. 2(b), B_{max} from our theoretical model (based on the Haines relativistic scaling[36]) are in accordance with that of PIC simulations. This indicates that our model is capable to quantitatively predict the magnetic field generation behind the target. It should be mentioned that the reason for the good agreement with the model results from Haines scaling is that the electrons cannot receive all energy from the ponderomotive potential with use of short fs level laser pulses,[38] and their temperature from PIC simulations is therefore is closer to that of Haines model predicted.

3. Enhancement of magnetic field from laser pulse interaction with grating target

From the magnetic field generation model established above, we can see that it is possible to enhance the strength of magnetic fields by increasing the hot-electron temperature. For short fs laser pulse interacting with solid target, strong laser reflection is unbeneficial for light absorption and thus the hot-electron temperature is rather limited. Micro-structured plasma grating targets have been widely used to enhance energy coupling between laser and solid targets, improve the effects of electron heating, charged-particle acceleration and radiation.[39–48] Here, we focus on the magnetic field generation from laser-driven grating target. The grating is a sinusoidal modulated grating structure placed on the front surface of solid target, as shown in Fig. 5(a). Its height is $h = 0.5$ μm and the period of sinusoidal structure is $l = 2.0$ μm. Other parameters are the same as the above simulation in Section 2.2. For comparison, the transverse profile of magnetic field and spectrum of hot electrons are also shown in Figs. 5(b) and 5(c).

Figure 5(b) shows the spatial distribution of self-generated magnetic field B_z at $t = 26T_0$ for both the cases with and without grating structure. We can see that, with use of surface grating, the strength of B_z behind the target is as high as 2.8×10^2 MG, which is about 2 times higher than that in the flat target case. This is attributed to the fact that the hot electrons can be heated to a higher temperature due to more efficient energy coupling, as seen in Fig. 5(a). Further, we also note that the transverse width of B_z widens from 16 μm to 26 μm and B_z in the front of the target shows different interference patterns due to the modulation of plasma grating.

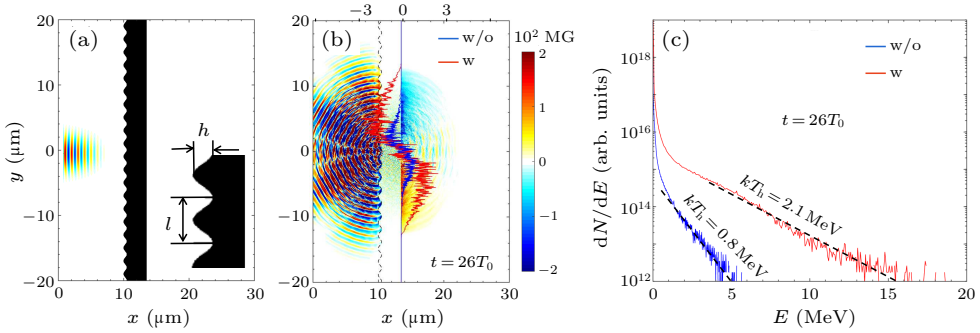


Fig. 5. (a) Schematic of relativistic laser pulse interacting with grating target (w). The inset gives a partial enlargement of grating target. (b) Distribution of self-generated magnetic field B_z at $t = 26T_0$ for both cases with (w) and without (w/o) grating structure. The red and blue curves represent its transverse profiles along the rear surface of grating target. (c) Spectra of electrons at $t = 26T_0$ for both the cases. The electron temperatures are labeled around the curves.

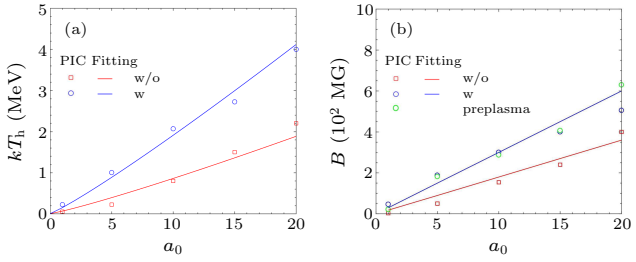


Fig. 6. Dependence of (a) the temperature of hot electrons kT_h and (b) the maximum strength of magnetic field behind the target B_z on the normalized laser amplitude a_0 for both the cases with (w) and without (w/o) the micro-structured grating. Here, red and blue symbols are the PIC simulation results, and red and blue lines represent their linear fittings. The green symbols are the simulation results with the preplasma of density $0.1n_c$ and thickness 1 μm in front of the substrate of grating target.

We next extend the laser intensity range to obtain the scaling laws of the maximum magnetic field strength B_{max}. Since B_{max} is positively correlated with kT_h in Eq. (13), the dependence of the B_{max} on a_0 is firstly given in Fig. 6(a). One can see that kT_h is proportional to a_0 for both the cases and kT_h has increased by more than 2 times by using a grating target. As a result, B_{max} is about two-fold enhanced, as shown in Fig. 6(b). This indicates that it is easy to achieve intense magnetic fields with strength $> 10^2$ MG and the enhancement effect for B_{max} with use of plasma grating is robust in a wide range of laser intensity. We then discuss the preplasma effect on B_{max} since it is inevitable even using modern laser cleaning techniques.

Figure 6(b) also shows the simulation results of laser interaction with a grating target with a preplasma of density $0.1n_c$ and thickness 1 μm in front of the substrate. One can see that the enhancement effect of magnetic field is still significant in the presence of the preplasma. However, for longer and non-uniform preplasmas, the mechanism of magnetic field generation still needs further research since Betatron-like resonance heating[49] may become dominant.

4. Parametric effect and robustness of the magnetic field enhancement regime

Figures 7(a) and 7(b) show the transverse profiles of magnetic field at the rear surface of the grating target for different incidence angle α of laser pulse. From Fig. 7(a), one can see that the magnetic field exhibits a typically asymmetrical distribution due to the oblique incidence of the laser. In addition, we find that kT_h and B_{max} are highest at $\alpha = 45^\circ$ in Fig. 7(d) since the field intensity after laser interference is most intense in this case.[50] It should be mentioned that, for the sinusoidal grating, surface plasma waves (SWs) will be generated to promote the laser absorption if the grating period, electron density and the incidence angle satisfy the resonant coupling condition[51]

$$\sin\alpha + \frac{\lambda}{l} = \sqrt{\left(1-\frac{n_e}{n_c}\right)\left(2-\frac{n_e}{n_c}\right)}. \tag{14}$$

For the laser-grating parameter given above, SWs can be excited at $\alpha = 30^\circ$. In contrast, we find that SWs are not as good as the interference effect $\alpha = 45^\circ$ for achieving higher kT_h and B_{max}.

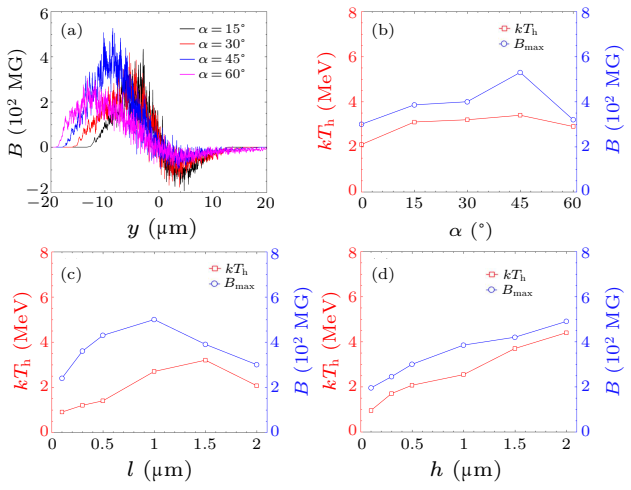


Fig. 7. Temperature of hot electrons (the left red y-axis) and the maximum strength of magnetic field B_{max} (the right blue y-axis) versus (a) the period l and (b) height h of plasma grating. Temperature of hot electrons (the left red y-axis) and the maximum strength of magnetic field B_{max} (the right blue y-axis) versus (c) the period l and (d) height h of plasma grating.

The grating size and the incidence angle of laser pulse play an important role in the magnetic field generation. We firstly examine the effect of grating period l on kT_h and B_{max}, as shown in Fig. 7(c). One can see that the optimal grating period is at about $l = 1$ μm for effective electron heating and thus intense magnetic field generation, which is in good accordance with our previous simulation and theoretical results.[52] This is due to the fact that more localized electromagnetic fields can be excited inside the gaps between the gratings, which is beneficial for laser absorption and electron heating.[52] The grating height h is also crucial for the magnetic field generation. Figure 7(d) shows that hot electrons are heated to a higher temperature, and stronger magnetic fields can be generated with increasing h due to longer acceleration length. It is worth noting that for gratings larger than 1 μm in height, plasma grating actually behaves like multiple plasma channels.[38,52,53] Attosecond electron bunches can be pulled out from the inner walls of the grating surfaces by the transverse electric fields and may be accelerated by the longitudinal electric field of transverse magnetic mode excited inside the plasma channels.[38,52,53] When energetic dense electron bunches cross the rear surface of the target, self-generated annular magnetic fields can also be induced. The slight difference is that the radial return current J_r is greatly reduced since these electrons have very large longitudinal momentum.[38,52,53]

5. Methods

PIC simulation Simulations are performed by using the well-known PIC code EPOCH.[54] The simulation box is $x \times y = 100\lambda_0 \times 40\lambda_0$ with 5000×2000 cells, where $\lambda_0 = 1$ μm is the laser wavelength. Each cell contains 108 charged particles, including electrons, protons and C^{6+} ions. Open boundary conditions for both particles and fields are used at all boundaries. The initial target plasma is cold and its temperature is set to 0. In Figs. 6 and 7(a)–7(c), a_0, l, h, and α are changed in turn and other parameters remain the same as those in Subsection 2.3.

6. Conclusion

Magnetic field generation is one of basic physical phenomena in the relativistic laser pulse interacting with solid target. Hundreds-MG intense annular self-generated magnetic fields can be generated by the longitudinal electron current and radial electron return one. To summarize, we establish a theoretical model to quantitatively predict the spatial strength distribution of magnetic fields behind the target from the total current consisting of the above two directions, which agrees well with that in the simulations. Analytical results show that the strength of magnetic fields is positively associated with the hot-electron temperature. This provides us a way to improve the magnetic field characteristics. We propose to use surface grating structure in the front of solid target to improve hot-electron temperature and to enhance the magnetic field

strength. It is found that, for ultraintense ultrashort laser pulse, the magnetic field strength is several times increased with use of plasma grating, compared with the flat target case. The optimal grating period is at about one laser wavelength and the magnetic field strength becomes stronger with increasing grating height. It is possible to obtain asymmetrically distributed magnetic fields when the laser pulse is obliquely incident on the solid target. The strongest magnetic field appears at an incidence angle of 45° due to the localized electromagnetic fields from light interference. Our results may be useful for controlling charged particle transport and related explorations in laboratory astrophysics.

Acknowledgements

This work was supported by the National Natural Science Foundation of China (Grant Nos. 12175310, 12305268, and U2241281), the Natural Science Foundation of Hunan Province (Grant Nos. 2024JJ6184, 2022JJ20042, and 2021JJ40653), and the Scientific Research Foundation of Hunan Provincial Education Department (Grant Nos. 22B0655 and 22A0435).

References

[1] Tatarakis M, Watts I, Beg F N, Clark E L, Dangor A E, Gopal A, Haines M G, Norreys P A, Wagner U, Wei M S, Zepf M and Krushelnick K 2002 *Nature* **415** 280
[2] Tatarakis M, Gopal A, Watts I, Beg F N, Dangor A E, Krushelnick K, Wagner U, Norreys P A, Clark E L, Zepf M, Evans R G, *et al.* 2002 *Phys. Plasmas* **9** 2244
[3] Sarri G, Macchi A, Cecchetti C A, Kar S, Liseykina T V, Yang X H, Dieckmann M E, Fuchs J, Galimberti M, Gizzi L A, Jung R, Kourakis I, Osterholz J, Pegoraro F, Robinson A P L, Romagnani L, Willi O and Borghesi M 2012 *Phys. Rev. Lett.* **109** 205002
[4] Fujioka S, Zhang Z, Ishihara K, Shigemori K, Hironaka Y, Johzaki T, Sunahara A, Yamamoto N, Nakashima H, Watanabe T, Shiraga H, Nishimura H and Azechi H 2013 *Sci. Rep.* **3** 1170
[5] Wang W M, Gibbon P, Sheng Z M and Li Y T 2015 *Phys. Rev. Lett.* **114** 015001
[6] Nakamura D, Ikeda A, Sawabe H, Matsuda Y H and Takeyama S 2018 *Rev. Sci. Instrum.* **89** 095106
[7] Murakami M, Honrubia J J, Weichman K, Arefiev A V and Bulanov S V 2020 *Sci. Rep.* **10** 16653
[8] Park H S, Huntington C M, Fiuza F, *et al.* 2015 *Nat. Phys.* **11** 173
[9] Fiksel G, Fox W, Bhattacharjee A, Barnak D H, Chang P Y, Germaschewski K, Hu S X and Nilson P M 2014 *Phys. Rev. Lett.* **113** 105003
[10] Bulanov S V, Esirkepov T Zh, Kando M, Koga J, Kondo K and Korn G 2015 *Plasma Phys. Rep.* **41** 1
[11] Stamper J A, McLean E A and Ripin B H 1978 *Phys. Rev. Lett.* **40** 1177
[12] Strozzi D J, Tabak M, Larson D J, Divol L, Kemp A J, Bellei C, Marinak M M and Key M H 2012 *Phys. Plasmas* **19** 072711
[13] Sakata S, Lee S, Morita H, *et al.* 2018 *Nat. Commun.* **9** 3937
[14] Miyazaki S, Kawata S, Sonobe R and Kikuchi T 2005 *Phys. Rev. E* **71** 056403
[15] Pukhov A 2001 *Phys. Rev. Lett.* **86** 3562
[16] Chen H, Wilks S C, Meyerhofer D D, Bonlie J, Chen C D, Chen S N, Courtois C, Elberson L, Gregori G, Kruer W, Landoas O, Mithen J, Myatt J, Murphy C D, Nilson P, Price D, Schneider M, Shepherd R, Stoeckl C, Tabak M, Tommasini R and Beiersdorfer P 2010 *Phys. Rev. Lett.* **105** 015003
[17] Kopp R A and Pneuman G W 1976 *Sol. Phys.* **50** 85
[18] Masuda S, Kosugi T, Hara H, Tsuneta S and Ogawara Y 1994 *Nature* **371** 495
[19] Sudan R N 1993 *Phys. Rev. Lett.* **70** 3075
[20] Kolodner P and Yablonovitch E 1979 *Phys. Rev. Lett.* **43** 1402
[21] Stamper J A 1991 *Laser Part. Beam* **9** 841
[22] Haines M G 1997 *Phys. Rev. Lett.* **78** 254
[23] Bell A R, Davies J R and Guerin S M 1998 *Phys. Rev. E* **58** 2471
[24] Macchi A 2012 arXiv: 1202.0389
[25] Weichman K, Murakami M, Robinson A P L and Arefiev A V 2020 *Appl. Phys. Lett.* **117** 244101
[26] Nakatsutsumi M, Sentoku Y, Korzhimanov A, Chen S N, Buffechoux S, Kon A, Atherton B, Audebert P, Geissel M, Hurd L, Kimmel M, Rambo P, Schollmeier M, Schwarz J, Starodubtsev M, Gremillet L, Kodama R and Fuchs J 2018 *Nat. Commun.* **9** 280
[27] Moore C I, Knauer J P and Meyerhofer D D 1995 *Phys. Rev. Lett.* **74** 2439
[28] Kolodner P and Yablonovitch E 1979 *Phys. Rev. Lett.* **43** 1402
[29] Wilks S C, Langdon A B, Cowan T E, Roth M, Singh M, Hatchett S, Key M H, Pennington D, MacKinnon A and Snavely R A 2001 *Phys. Plasmas* **8** 542
[30] Gurevich A V, Pariiskaya L V and Pitaevskii L P 1966 *Sov. Phys. JETP* **22** 449
[31] Mora P 2003 *Phys. Rev. Lett.* **90** 185002
[32] Jackson J D 1999 *Classical Electrodynamics* (New York: Wiley) p. 833
[33] Tikhonchuk V T, Andreev A A, Bochkarev S G and Bychenkov V Y 2005 *Plasma Phys. Control. Fusion* **47** B869
[34] Robinson A P L, Bell A R and Kingham R J 2006 *Phys. Rev. Lett.* **96** 035005
[35] Beg F N, Bell A R, Dangor A E, Danson C N, Fews A P, Glinsky M E, Hammel B A, Lee P, Norreys P A and Tatarakis M 1997 *Phys. Plasmas* **4** 447
[36] Haines M G, Wei M S, Beg F N and Stephens R B 2009 *Phys. Rev. Lett.* **102** 045008
[37] Kluge T, Cowan T, Debus A, Schramm U, Zeil K and Bussmann M 2011 *Phys. Rev. Lett.* **107** 205003
[38] Zou D B, Pukhov A, Yi L Q, Zhuo H B, Yu T P, Yin Y and Shao F Q 2017 *Sci. Rep.* **7** 42666
[39] Gauthier J C J, Bastiani S, Audebert P, Geindre J P, Neuman K, Donnelly T D, Hoffer M, Falcone R W, Shepherd R L, Price D F and White W E 1995 *Proc. SPIE* **2523** 242
[40] Kupersztych J, Raynaud M and Riconda C 2004 *Phys. Plasmas* **11** 1669
[41] Raynaud M, Kupersztych J, Riconda C, Adam J C, Héron A, *et al.* 2007 *Phys. Plasmas* **14** 092679
[42] Hu G Y, Lei A L, Wang J W, Huang L G, Wang W T, Wang X, Xu Y, Shen B F, Liu J S, Yu W, Li R X and Xu Z Z 2010 *Phys. Plasmas* **17** 083102
[43] Lavocat-Dubuis X and Matte J P 2010 *Phys. Plasmas* **17** 093105
[44] Li Y T, Yuan X H, Xu M H, Zheng Z Y, Sheng Z M, Chen M, Ma Y Y, Liang W X, Yu Q Z, Zhang Y, Liu F, Wang Z H, Wei Z Y, Zhao W, Jin Z and Zhang J 2006 *Phys. Rev. Lett.* **96** 165003
[45] Wang W M, Sheng Z M and Zhang J 2008 *Phys. Plasmas* **15** 030702
[46] Hu G Y, Lei A L, Wang W T, Wang X, Huang L G, Wang J W, Xu Y, Liu J S, Yu W, Shen B F, Li R X and Xu Z Z 2010 *Phys. Plasmas* **17** 033109
[47] Klimo O, Psikal J, Limpouch J, Proska J, Novotny F, Ceccotti T, Floquet V and Kawata S 2011 *New J. Phys.* **13** 053028
[48] Kaw P K and McBride J B 1970 *Phys. Fluids* **13** 1784
[49] Pukhov A, Sheng Z M and Meyer-ter-Vehn J 1999 *Phys. Plasmas* **6** 2847
[50] Jiang X R, Shao F Q, Zou D B, Yu M Y, Hu L X, Guo X Y, Huang T W, Zhang H, Wu S Z, Zhang G B, Yu T P, Yin Y, Zhuo H B and Zhou C T 2020 *Nucl. Fusion* **60** 076019
[51] Raether H 1988 *Surface Plasmons on Smooth and Rough Surfaces and on Gratings*. In: *Springer Tracts in Modern Physics* (Berlin: Springer) vol. 111
[52] Zou D B, Yu D Y, Jiang X R, Yu M Y, Chen Z Y, Deng Z G, Yu T P, Yin Y, Shao F Q, Zhuo H B, Zhou C T and Ruan S C 2019 *Phys. Plasmas* **26** 123105
[53] Ji L L, Snyder J, Pukhov A, Freeman R R and Akli K U 2016 *Sci. Rep.* **6** 23256
[54] Ridgers C P, Brady C S, Duclous R, Kirk J G, Bennett K, Arber T D, Robinson A P L and Bell A R 2012 *Phys. Rev. Lett.* **108** 165006